

UCLA

UCLA Previously Published Works

Title

Stability of trivalent and hexavalent chromium oxide layers on aluminum substrates from electronic structure calculations

Permalink

<https://escholarship.org/uc/item/61s5q2mz>

Journal

Physical Review Materials, 8(11)

ISSN

2476-0455

Authors

Geng, Peng

Huang, Shu

Marian, Jaime

Publication Date

2024-11-01

DOI




10.1103/physrevmaterials.8.113603

Copyright Information

This work is made available under the terms of a Creative Commons Attribution License, available at <https://creativecommons.org/licenses/by/4.0/>

Peer reviewed

Stability of trivalent and hexavalent chromium oxide layers on aluminum substrates from electronic structure calculations

Peng Geng¹,,* Shu Huang¹,, and Jaime Marian^{1,2},

¹Department of Materials Science and Engineering, University of California, Los Angeles, California, United States

²Department of Mechanical and Aerospace Engineering,
University of California, Los Angeles, California, United States

(Dated: November 16, 2024)

Aluminum's light weight and high-strength make it a highly desirable material as a structural material in the transportation sector. However, its relatively high corrosion susceptibility poses challenges for its wide application under exposure to the elements. Traditionally, hexavalent chromium (VI) oxide (CrO_3) coatings have been employed to provide corrosion protection, but their toxicity and environmental impact have motivated research to seek less harmful options. Trivalent chromium (III) oxide (Cr_2O_3) suggests itself as a natural alternative due to its similar chemistry and lower toxicity. However, the stability of its bonding to pure Al metal substrates has not been thoroughly investigated. This study focuses on calculations of the adhesion work (W_{ad}) and interface energy (γ_{ij}) of Al/ CrO_3 and Al/ Cr_2O_3 interface structures with different Al crystallographic orientations ((100), (110), and (111)) using density functional theory (DFT) calculations. Significant variations in the adhesion work W_{ad} and interface energy γ_{ij} were observed for Al/ CrO_3 interface structures across different Al planes, primarily attributed to the formation of interpenetrating Al-Cr oxide substructures and the formation of Al-O-Al bonds within the interface region. In contrast, the Al/ Cr_2O_3 interface energies exhibited a relatively weak dependence on the metal substrate orientation, with well-defined oxide and metallic layers and no oxygen penetration into the aluminum. Notably, Al/ Cr_2O_3 interfaces generally displayed higher adhesion work W_{ad} and lower interface energy γ_{ij} compared to Al/ CrO_3 , suggesting that Cr_2O_3 forms more stable interfaces and adheres more strongly to Al. These findings contribute to the development of sustainable corrosion protection solutions in the aerospace and marine industries by highlighting the potential of Cr_2O_3 coatings as a viable environmentally friendly alternative to CrO_3 .

Keywords: adhesion work, interface energy, Al/ CrO_3 interface, Al/ Cr_2O_3 interface

I. INTRODUCTION

The transportation industry has long relied on lightweight materials to optimize fuel efficiency and enhance performance in aircraft, spacecraft, road vehicles, and marine vessels. Aluminum has become an attractive choice due to its exceptional strength-to-weight ratio, intrinsic corrosion resistance, and abundance. In the aerospace sector, aluminum is still extensively utilized for constructing various components in commercial airliners, spacecraft, and vehicle fuselages, as well as engine components, enabling reduced fuel consumption and increased payload capacity [1–4]. Similarly, in the marine industry, aluminum's corrosion-resistant properties and durability make it an ideal material for boat hulls, vessel equipment, and marine infrastructure, performing effectively in aggressive marine environments [5, 6]. In the automotive sector, aluminum has typically been used only in high-end vehicles, being less strong and more expensive than steel [7, 8], although its use keeps expanding thanks to modern Al grades with enhanced strength, efficient recyclability, and lower weight.

The corrosion resistance of aluminum is attributed to the intrinsic passivating character of aluminum oxide. When aluminum is exposed to air or other oxidizing environments, its strong affinity for oxygen leads to the rapid formation of a thin oxide film on the surface [9, 10]. This film is chemically stable and acts as an effective barrier to oxygen diffusion, making it resistant to chemical reactions with most substances,

including acids, bases, and salts. The stability of this thin film prevents corrosive ions from breaking down or dissolving the underlying aluminum through the oxide layer when exposed to corrosive environments [11–13]. Additionally, the hard and dense nature of the aluminum oxide film provides mechanical protection to the underlying aluminum by resisting scratching, abrasion, and wear [14, 15]. However, the initial oxide layer formed upon exposure to air or water is extremely thin, often only a few nanometers thick, limiting its corrosion resistance and mechanical protection to ambient conditions [16]. The $4 < \text{PH} < 7$ corrosion protection range also restricts its use in aerospace and marine applications, which often involve severe environments or extremely harsh conditions [9, 16].

To mitigate the effects of corrosion and extend the lifespan of aluminum components, the aerospace and marine sectors have traditionally employed hexavalent chromium (VI) oxide (CrO_3) coatings through the dipping process known as Chromate Conversion Coating (CCC). In this process, aluminum is immersed in a chemical bath containing chromates or dichromates (e.g., BaCrO_4 or $\text{K}_2\text{Cr}_2\text{O}_7$) to form the CCC film [17–19]. This film can inhibit oxygen reduction reactions, increase film resistance, and restore unreacted Cr (VI) (Cr^{6+}) ions for self-healing [19–21]. The unreacted Cr^{6+} ions act as a reservoir, regenerating the protective oxide film when the aluminum surface is exposed through film cracks or defects [19]. Thus, the CCC film serves as an effective barrier against corrosion, safeguarding aluminum structures from environmental degradation and ensuring the integrity of critical components. However, the widespread use of CrO_3 coatings has raised significant health and environmental concerns due

* Corresponding author: penggeng@ucla.edu

to its toxic and carcinogenic nature, causing severe health hazards such as lung cancer, skin irritation, and respiratory problems [22, 23].

In response to growing environmental consciousness and regulatory scrutiny, there is increased interest in finding alternative materials that offer comparable corrosion resistance without the associated health and environmental risks posed by CrO₃. Trivalent chromium (III) oxide (Cr₂O₃) has emerged as a promising candidate for replacing CrO₃ coatings due to its lower toxicity and potential for environmentally friendly application processes [19]. The Trivalent Chromium Process (TCP) was developed as an alternative to the traditional CCC process, utilizing chromium (III) chloride or chromium (III) sulfate in the chemical bath to produce the oxide film containing only chromium (III) (Cr³⁺) ions [24, 25]. This film has demonstrated comparable corrosion resistance and even better high-temperature and oxidative environment resistance compared to Cr⁶⁺ films [21, 24–26]. However, concerns have arisen regarding the possible re-oxidation of Cr³⁺ to Cr⁶⁺ during prolonged exposure to air or immersion in sodium chloride solution [26, 27]. To circumvent this issue, the physical vapor deposition (PVD) technique has been used to produce the Cr₂O₃ coatings, as this non-solution process eliminates the risk of Cr⁶⁺ formation [27]. Although several methods have been explored to produce Cr₂O₃ coatings, achieving strong adhesion between the coating and the aluminum surface remains challenging, potentially leading to delamination and reduced coating effectiveness.

While the kinetics of oxide film chemistry and formation may be nontrivial, atomistic calculations can provide fundamental information about the properties and structure of metal/oxide interfaces [28–31]. However, despite its importance, no Cr-oxide/Al-metal interface property calculations exist in the literature. In this paper, we carry out a comprehensive investigation of the stability of Cr oxide films on crystalline Al substrates by calculating the adhesion work, W_{ad} , and interface energies, γ_{ij} , of Al/CrO₃ and Al/Cr₂O₃ interfaces with different crystallographic orientations. We use density functional theory (DFT) calculations to calculate all the necessary parameters needed to obtain these critical interfacial properties. Further, we conduct a detailed configurational study of the final metal/oxide atomic structures to gain insight into the formation mechanism of the various interfaces and their relation to W_{ad} and γ_{ij} . More broadly, our objective is to determine whether trivalent Cr oxide films can be suitable replacements for hexavalent ones from an atomic perspective. This study may thus contribute to the development of sustainable corrosion protection solutions for the aerospace and marine industries, providing valuable guidance toward enhancing the environmental sustainability and performance of aluminum-based structures in aircraft, spacecraft, and marine vessels.

II. METHODOLOGY

A. Adhesion work and interface energy functions

In this work, we calculate two main interface properties: the adhesion work W_{ad} and the interface energy γ_{ij} . These two properties play a crucial role in determining the structural integrity of the interface between two layers of dissimilar materials. The adhesion work W_{ad} is defined as the minimum amount of force required to separate two bonded materials by an infinitesimal distance. W_{ad} is thus essential for quantifying the adhesion and bonding strength between two surfaces. Notably, W_{ad} is directly correlated with the fracture strength σ_F and fracture toughness K_c of the material, as defined by Griffith's criterion and the expression for the fracture toughness. Griffith's equation predicts crack propagation when the stress of the largest crack in the material exceeds the critical fracture stress σ_F :

$$\sigma_F = \sqrt{\frac{EW_{\text{ad}}}{\pi c}} \quad (1)$$

where E is Young's modulus and c is the half-crack length [32, 33]. Additionally, the expression for the fracture toughness, $K_c = \sqrt{EW_{\text{ad}}}$, quantifies the amount of energy required to propagate the crack [32, 34]. In our calculations, the adhesion work is obtained as [33, 35–38]:

$$W_{\text{ad}} = \frac{E_m + E_{\text{ox}} - E_{\text{m/ox}}}{A_i} \quad (2)$$

where E_m is the energy of a relaxed Al free surface, E_{ox} is the energy of a relaxed Cr oxide free surface, $E_{\text{m/ox}}$ is the total energy of the relaxed interface model between Al and CrO₃ or Cr₂O₃, and A_i is the surface area of the interface.

For its part, γ_{ij} is the extra energy associated with joining two dissimilar materials, i and j , across a planar interface. A negative value of γ_{ij} indicates a drop in energy when two open surfaces of dissimilar materials are combined to form a joint interface. Understanding γ_{ij} is essential for various applications, including adhesion, surface phenomena, catalysis, and composite material formation. Despite its significance, no experimental data exist for Al/CrO₃ and Al/Cr₂O₃ interfaces. γ_{ij} is typically calculated relative to the bulk free energies of the constituent materials, using the following expression [33, 39, 40]:

$$\gamma_{ij} = \frac{E_{ij} - E_i - E_j}{A_{ij}} \quad (3)$$

where E_{ij} is the total energy of the relaxed interface region, E_i is the total energy of bulk Al, E_j is the total energy of bulk CrO₃ or Cr₂O₃, and A_{ij} is the surface area of the interface. Although eq. (3) represents the standard formulation for calculating the interface energy γ_{ij} , accurately determining the total energy of the relaxed interface region E_{ij} in small computational supercells remains a challenge. Here, we employ an alternative formulation to calculate γ_{ij} [33, 41, 42]:

$$\gamma_{ij} = \gamma_s^{\text{m}} + \gamma_s^{\text{ox}} - W_{\text{ad}} \quad (4)$$

where γ_s^m is the surface energy of the Al (metal) plane in contact with the CrO_3 or Cr_2O_3 slab, and γ_s^{ox} is the surface energy of the CrO_3 or Cr_2O_3 (oxide) plane in contact with the Al slab.

The surface energy γ_s is the fundamental property that characterizes the stability of solid surfaces, representing the excess energy associated with atoms or molecules present at the solid surface compared to those in the bulk material. To calculate the surface energy γ_s of the Al and CrO_3 or Cr_2O_3 plane in contact with each other, we use the following equation [43]:

$$\gamma_s = \frac{1}{2A_s}(E_{\text{slab}}^{\text{ur}} - NE_b) + \frac{1}{A_s}(E_{\text{slab}}^{\text{r}} - E_{\text{slab}}^{\text{ur}}) \quad (5)$$

where A_s is the surface area, $E_{\text{slab}}^{\text{ur}}$ and $E_{\text{slab}}^{\text{r}}$ are the unrelaxed and relaxed total energy of the slab, respectively, N is the number of Al atoms or number of CrO_3 or Cr_2O_3 molecules in the slab, and E_b is the bulk energy per atom for the Al slab or the bulk energy per molecule for the CrO_3 or Cr_2O_3 slab.

B. Density functional theory calculations

Atomistic simulations capable of capturing metallic/ceramic chemistry can be challenging and must generally be based on first principles calculations for accuracy. Density functional theory (DFT) calculations were performed using the *Vienna Ab initio Simulation Package* (VASP-v5.4.4) [44–49], with GPU acceleration enabled [50, 51]. Structure visualization was performed with *Visualization for Electronic and Structural Analysis* (VESTA) software [52]. The electronic structure calculations were carried out with the Perdew-Burke-Ernzerhof (PBE) exchange-correlation function based on the generalized gradient approximation (GGA) [53, 54]. To incorporate van der Waals (vdW) dispersion effects, the DFT-D3 correction scheme with the Becke-Johnson damping function was employed in the DFT calculations [54, 55]. The plane-wave basis set was truncated at an energy cutoff of 550 eV for the expansion of the wave functions. The Conjugate Gradient (CG) algorithm was utilized to achieve ion relaxation, ensuring that the ions reached their respective ground states in our calculations. We applied a force convergence criterion of 2×10^{-2} eV/Å during structural relaxation and a tolerance of 10^{-5} eV for the energy during electronic relaxation. For unit cell optimization, a stricter convergence criterion was implemented, utilizing 10^{-4} eV/Å for the forces and 10^{-6} eV for the energies. For pure Al, partial occupancies for each orbital were determined using the second-order Methfessel-Paxton, occasionally using third- or fourth-order iterations to ensure the entropy term remained below 1 meV/atom. For pure CrO_3 and Cr_2O_3 , partial occupancies for each orbital were determined using the Blochl-corrected tetrahedron method. When it came to interface models, the Gaussian smearing method with a width of 0.05 was adopted to determine partial occupancies for each orbital. To treat the presence of the dipole moment along the c direction for slab and interface models, a correction for the potential arising from the dipole moment was applied in the calculations. The ‘accurate’ precision mode was used, resulting in a denser grid that mitigates egg-box effects,

avoids aliasing errors, and improves the augmentation of wave functions, thereby enhancing numerical accuracy. The computational efficiency was enhanced by employing a mixed strategy that combined the blocked-Davidson and RMM-DIIS electronic minimization algorithms, while the real-space projection operators were automatically optimized to reduce the computational cost without sacrificing the accuracy of the results [47, 48]. The Brillouin zone in k -space was centered at the gamma point, preserving the complete symmetry of the space group. The regular k -point mesh was employed with subdivisions based on the ratios of lattice vector magnitudes, ensuring consistent spacing that adapts to changes in lattice orientation.

The interface models were constructed based on the experimental unit cell structures of Al, CrO_3 , and Cr_2O_3 . The unit cells of Al, CrO_3 , and Cr_2O_3 with (100) free surfaces were obtained from the *Inorganic Crystal Structure Database* (ICSD) [56]. The geometry optimized unit cell structure of Al with (100), (110), and (111) exposed surfaces are shown in Fig. 1(a)-(c). For CrO_3 and Cr_2O_3 , the unit cell structures were geometrically optimized to obtain their relaxed configurations, as shown in Figs. 1(d) and 1(e), respectively. We note that CrO_3 and Cr_2O_3 crystallize in orthorhombic and hexagonal crystal structures, respectively.

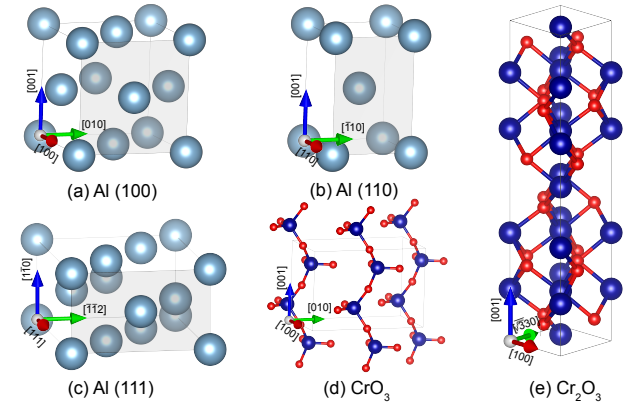


FIG. 1. Bulk crystal structures and unit cells used in the DFT calculations. (a) Al with (100) plane exposed. (b) Al with (110) plane exposed. (c) Al with (111) plane exposed. (d) CrO_3 with (100) plane exposed. (e) Cr_2O_3 with (100) plane exposed. In (a)-(c), the shaded plane indicates the exposed plane. Gray-blue, red, and dark blue colored atoms are aluminum, oxygen, and chromium atoms, respectively. The unit cell crystal directions are annotated in each crystal structure.

To construct the interface models, the lattice parameters along the a and b directions for Al and CrO_3 or Cr_2O_3 were calculated and compared to ensure minimal lattice mismatch at the interface while maintaining computational feasibility. Table I presents six interface models, along with their respective final determined interface lattice constant along the a and b directions. Additionally, Table I shows the lattice mismatch between the interface lattice constant and those of the Al, CrO_3 , or Cr_2O_3 slabs along a and b . It is important to note that the reported lattice mismatch in Table I is only for the Al slab

and not for the CrO_3 or Cr_2O_3 slab. This approach is adopted because Al exhibits significantly higher ductility compared to CrO_3 and Cr_2O_3 , allowing the Al slab to be compressed or stretched more readily in reality. Consequently, adjusting the Al slab solely minimizes the strain effect and improves computation accuracy when compared to compressing or stretching both Al and CrO_3 or Cr_2O_3 slabs. As shown in Table I, the maximum lattice mismatch for the Al slab is 8.05%, indicating a reasonably small degree of mismatch at the interface planes.

Utilizing the interface lattice constants from Table I and the unit cell structures depicted in Fig. 1, six interface models were constructed: Al(100)/ CrO_3 (100), Al(100)/ Cr_2O_3 (100), Al(110)/ CrO_3 (100), Al(110)/ Cr_2O_3 (100), Al(111)/ CrO_3 (100), and Al(111)/ Cr_2O_3 (100) (see Fig. 2). In all cases, an Al slab containing seven atomic layers is positioned at the bottom with the three bottommost atomic layers fixed to the bulk crystal lattice positions. The oxide slabs are placed at a distance from Al, corresponding to the lowest single-point calculation energy. Additionally, a 15 Å vacuum region is introduced above the CrO_3 or Cr_2O_3 slab to create a non-periodic environment. We define the interface region as composed of the two atomic layers closest to the oxide-metal junction on each side (the metal and the oxide).

III. RESULTS

A. Adhesion work and interface energy calculations

1. Metal/oxide adhesion work

To calculate the adhesion work W_{ad} defined in eq. (2), the interface models illustrated in Fig. 2 were directly used to obtain the total energy of the relaxed interface model $E_{\text{m/ox}}$. The total energy of Al slab E_{m} was calculated by removing the CrO_3 or Cr_2O_3 slab from the interface model. Similarly, the total energy of CrO_3 or Cr_2O_3 slab E_{ox} was calculated by removing the Al slab from the interface model. It is important to note that the three bottommost atomic layers in the Al slab were fixed to ensure the E_{m} energies were calculated correctly, consistent with the setup of the interface model. Following the DFT calculation procedure described in Section II B, the total energy of the relaxed interface model $E_{\text{m/ox}}$, the total energy of the relaxed strained Al slab E_{m} , and the total energy of the relaxed CrO_3 or Cr_2O_3 slab E_{ox} were calculated, as reported in Table II. The cross-sectional area of the interface A_i was determined using the interface lattice constant a and b listed in Table I. Employing these data and eq. (2), the adhesion work for the six different interface models is calculated and presented in Table II. For the Al/ CrO_3 interface models, the adhesion work exhibits significant variations across different crystallographic orientations. In particular, there is a significant difference of $0.121 \text{ eV}\cdot\text{\AA}^{-2}$ (65.8%) between Al(100)/ CrO_3 (100) and Al(110)/ CrO_3 (100), and a slightly larger difference of $0.033 \text{ eV}\cdot\text{\AA}^{-2}$ (17.9%) between Al(100)/ CrO_3 (100) and Al(111)/ CrO_3 (100). In con-

trast, the adhesion work for the Al and Cr_2O_3 interface displays a smaller difference trend across different crystallographic orientations. Specifically, a relatively small difference of $0.021 \text{ eV}\cdot\text{\AA}^{-2}$ (8.3%) is observed between Al(100)/ Cr_2O_3 (100) and Al(110)/ Cr_2O_3 (100) models, and an even smaller difference of $0.003 \text{ eV}\cdot\text{\AA}^{-2}$ (1.2 %) is detected between Al(100)/ Cr_2O_3 (100) and Al(111)/ Cr_2O_3 (100) models. When comparing the adhesion work W_{ad} between Al/ CrO_3 and Al/ Cr_2O_3 with identical Al slab orientation, Al/ Cr_2O_3 exhibits higher values than Al/ CrO_3 for the Al (100) and (111) planes, while for the Al (110) plane, Al/ Cr_2O_3 displays lower values compared to Al/ CrO_3 . Both Al/ CrO_3 and Al/ Cr_2O_3 exhibit the highest adhesion work W_{ad} with the Al (110) plane.

2. Al surface energies

To calculate the interface energy γ_{ij} between Al and CrO_3 or Cr_2O_3 following the eq. (4), it is necessary first to determine the surface energy of the Al plane, γ_s^{m} , in contact with the CrO_3 or Cr_2O_3 slab, as well as the surface energy of the CrO_3 or Cr_2O_3 plane, γ_s^{ox} , in contact with the Al plane using eq. (5). Following eq. (5) to calculate the surface energy of the Al plane, γ_s^{m} , the bulk energy per atom for Al, E_{b} , were determined using the optimized Al unit cell structure with (100), (110), and (111) orientations, as illustrated in Fig. 1(a)-(c). The number of atoms in the Al slab N was counted from the atomic model employed in the construction of each interface model. The unrelaxed total energy of the unstrained Al slab, $E_{\text{slab}}^{\text{ur}}$, was calculated using the single-point energy calculation method without performing any relaxation. The relaxed total energy of the unstrained Al slab, $E_{\text{slab}}^{\text{r}}$, was determined by allowing the unstrained Al slab to be relaxed. Consistent with the interface model setup, the three bottommost atomic layers in the Al slab were kept fixed during the energy minimization to ensure an accurate representation of a metallic substrate. All the relevant variables, including the Al slab surface lattice parameters required in eq. (5), are listed in Table III. By examining the surface energy of unstrained Al slab γ_s^{m} listed in Table III, it is observed that the energy differences between the Al(100)/ CrO_3 (100) and Al(100)/ Cr_2O_3 (100) models, the Al(110)/ CrO_3 (100) and Al(110)/ Cr_2O_3 (100) models, and the Al(111)/ CrO_3 (100) and Al(111)/ Cr_2O_3 (100) models are relatively small, with values of $0.001 \text{ eV}\cdot\text{\AA}^{-2}$ (1.2%), $0 \text{ eV}\cdot\text{\AA}^{-2}$ (0%), and $0.001 \text{ eV}\cdot\text{\AA}^{-2}$ (1.3%), respectively. These small energy differences reinforce the robustness of the calculation method.

3. Comparison of Al slab energies to published results

Before proceeding with the analysis of the results, it is helpful to compare our calculated values with existing published works in the literature. To this end, we compare the surface energies of unstrained Al slabs, γ_s^{m} , with previously reported values with the same crystallographic orientations. The values from the last column in Table III are converted to $\text{J}\cdot\text{m}^{-2}$ and

TABLE I. Three leftmost columns: interface dimensions along the a and b directions for six interface models. Four rightmost columns: lattice mismatch between the interface models and the Al, CrO_3 , or Cr_2O_3 slabs.

Interface structure	Lattice constant a (Å)	Lattice constant b (Å)	Mismatch (–: compressed, +: stretched)			
			Al slab		Oxide slab	
			a (%)	b (%)	a (%)	b (%)
Al(100)/ CrO_3 (100)	8.42	11.48	+5.51	–4.02	0.00	0.00
Al(100)/ Cr_2O_3 (100)	7.86	14.67	–1.42	–8.05	0.00	0.00
Al(110)/ CrO_3 (100)	8.42	11.48	+5.51	+1.80	0.00	0.00
Al(110)/ Cr_2O_3 (100)	7.86	14.67	–7.06	–8.05	0.00	0.00
Al(111)/ CrO_3 (100)	25.25	5.74	+3.38	+1.80	0.00	0.00
Al(111)/ Cr_2O_3 (100)	14.67	7.86	+0.11	–7.06	0.00	0.00

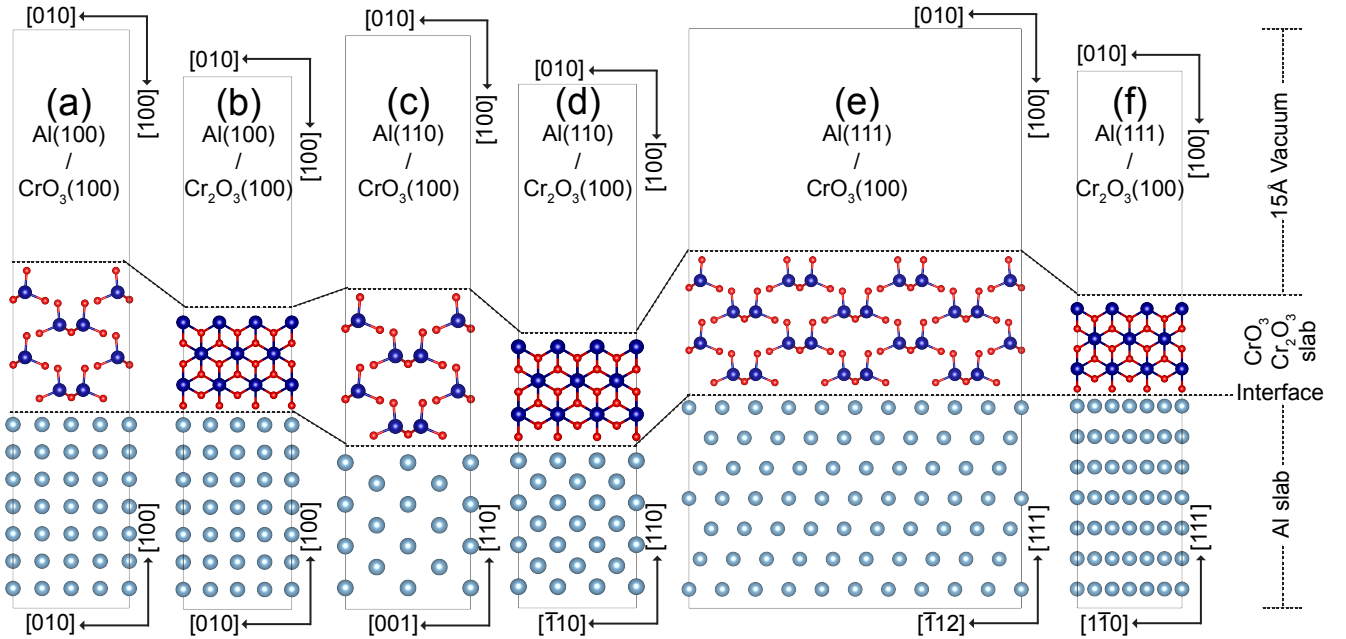


FIG. 2. Constructed interface models of Al/ CrO_3 or Al/ Cr_2O_3 . (a) Al(100)/ CrO_3 (100) interface model. (b) Al(100)/ Cr_2O_3 (100) interface model. (c) Al(110)/ CrO_3 (100) interface model. (d) Al(110)/ Cr_2O_3 (100) interface model. (e) Al(111)/ CrO_3 (100) interface model. (f) Al(111)/ Cr_2O_3 (100) interface model. Gray-blue, red, and dark blue colored atoms are aluminum, oxygen, and chromium atoms, respectively. The orientations of the Al, CrO_3 , and Cr_2O_3 slabs are indicated within each interface model. The structures of each interface model are delineated with dashed lines and annotated vertically on the right side.

shown in Table IV. It has been reported that the Full Charge Density (FCD) method can achieve comparable accuracy to the Local Density Approximation (LDA) method [57]. Patra *et al.* [58] has reported that the PBE method tends to underestimate surface energies by approximately 25%, while the PBE for solid (PBEsol) and strongly constrained and appropriately normed (SCAN) methods provide more accurate results compared to PBE, but are not as precise as the LDA method. Additionally, they highlighted that the SCAN + revised Vydrov–van Voorhis 2010 (rVV10) method stands as the most sophisticated non-empirical semi-local function

available presently [58]. Consequently, for the theoretical reference data, we have excluded surface energy values calculated using the PBE, PBEsol, and SCAN methods and primarily focused on comparing our results with those obtained from the LDA, SCAN+rVV10, and FCD methods, which are considered more reliable. In terms of experimental data, these surface energies can be extrapolated from polycrystalline surface tension measurements, which are also shown in Table IV. Overall, good agreement with both calculated and experimental data is seen, which adds confidence to the values calculated in this work.

TABLE II. Calculated adhesion work of six Al/CrO₃ or Al/Cr₂O₃ interface models using the relaxed interface model energy, single strained Al slab energy, single CrO₃ or Cr₂O₃ slab energy, and interface size (in Table I).

Interface structure	Combined energy (eV)	Energy of Al slab (eV)	Energy of oxide slab (eV)	Adhesion work (eV·Å ⁻²)
Al(100)/CrO ₃ (100)	-845.123	-326.548	-500.752	0.184
Al(100)/Cr ₂ O ₃ (100)	-1208.511	-433.166	-746.273	0.252
Al(110)/CrO ₃ (100)	-741.385	-211.156	-500.749	0.305
Al(110)/Cr ₂ O ₃ (100)	-1093.387	-315.633	-746.226	0.273
Al(111)/CrO ₃ (100)	-1331.264	-548.669	-751.141	0.217
Al(111)/Cr ₂ O ₃ (100)	-1267.676	-492.655	-745.628	0.255

TABLE III. Surface energies of (100), (110), and (111) Al surfaces were calculated from six unstrained Al slabs, which were utilized in constructing the Al/CrO₃ or Al/Cr₂O₃ interface models. The surface energy calculation involves determining the (i) per atom energy from bulk Al, (ii) the number of atoms in each unstrained Al slab, (iii) unrelaxed Al slab energy, (iv) relaxed Al slab energy, and (v) surface area.

Interface structure	Cohesive energy of Al (eV/atom)	Number of atoms in Al slab	Energy of unrelaxed Al slab (eV)	Energy of relaxed Al slab (eV)	Lattice constant <i>a</i> (Å)	Lattice constant <i>b</i> (Å)	Surface energy of Al slab (eV·Å ⁻²)
Al(100)/CrO ₃ (100)	-4.094	84	-327.758	-327.799	7.98	11.96	0.084
Al(100)/Cr ₂ O ₃ (100)	-4.094	112	-436.432	-436.652	7.98	15.95	0.085
Al(110)/CrO ₃ (100)	-4.076	56	-212.703	-212.851	7.98	11.28	0.085
Al(110)/Cr ₂ O ₃ (100)	-4.076	84	-319.056	-319.280	8.46	15.95	0.085
Al(111)/CrO ₃ (100)	-4.097	140	-551.716	-551.735	24.42	5.64	0.079
Al(111)/Cr ₂ O ₃ (100)	-4.097	126	-496.736	-496.794	14.65	8.46	0.078

TABLE IV. Comparison between the calculated aluminum surface energy from each unstrained Al slab computed in this work and in published computational and experimental studies. For each Al slab surface orientation, our work includes results for the two oxide substructures. All energies are given in J·m⁻².

Interface structure	This work	Calculated	Experimental
Al(100)/CrO ₃ (100)	1.348	1.347 ^a ,	1.28 ^e , 1.14 ± 0.2 ^f , 1.27 ^g
Al(100)/Cr ₂ O ₃ (100)	1.363	1.18 ^b , 1.15 ^c , 1.375 ^d	
Al(110)/CrO ₃ (100)	1.356	1.271 ^a ,	
Al(110)/Cr ₂ O ₃ (100)	1.356	1.19 ^b , 1.09 ^c	
Al(111)/CrO ₃ (100)	1.273	1.199 ^a ,	
Al(111)/Cr ₂ O ₃ (100)	1.256	1.11 ^b , 0.99 ^c , 1.27 ^h	

^a Full Charge Density Linear Muffin-Tin Orbitals (FCD-LMTO), Generalized Gradient Approximation (GGA) [57]^b Strongly Constrained and Appropriately Normed (SCAN) + revised Vydrov-van Voorhis 2010 (rVV10), meta-GGA [58]^c Local Density Approximation (LDA) [58]^d Mie-Lennard-Jones potential with analytical model [59]^e Extrapolation from surface tension measurements [60]^f Extrapolation from surface tension measurements [61]^g Extrapolation from surface tension measurements [62]^h Tight-Binding LMTO (TB-LMTO), LDA [63]

4. Oxide surface energies

To calculate the surface energy of the CrO₃ or Cr₂O₃ planes, γ_s^{ox} , using eq. (5), a procedure similar to that employed for determining the surface energy of the Al slab was utilized. We calculate the per molecule cohesive (bulk) energies of each oxide structure using the unit cells of the corresponding crystal structures, as shown in Fig. 1(d) and 1(e). Table V lists all the required variables, including the lattice parameters of the CrO₃ and Cr₂O₃ structures used to calculate γ_s^{ox} with eq. (5). As shown in the last column of Table V, the surface energies of the same oxide surface are the same regardless of the metal substrate crystal orientation (0.009 eV·Å⁻² for CrO₃ and 0.039 eV·Å⁻² for Cr₂O₃). This consistency across different interface configurations confirms the robustness and accuracy of the calculated results.

5. Metal/oxide interface energies

With all the calculations needed to obtain γ_{ij} in eq. (4) compiled in Tables II, III, and V, we list the resulting values in Table VI (to facilitate a direct comparison between W_{ad} and γ_{ij} , the values of W_{ad} originally presented in Table II are also included in Table VI). For the Al/CrO₃ inter-

TABLE V. Surface energies of (100) CrO_3 and Cr_2O_3 surfaces calculated from six unstrained CrO_3 and Cr_2O_3 slabs, which were used to construct the interface models of Al/CrO_3 or $\text{Al}/\text{Cr}_2\text{O}_3$. The surface energy calculation depends on (i) the bulk energy of the CrO_3 or Cr_2O_3 structures (expressed per molecule), (ii) the number of molecules in each unstrained slab, (iii) the unrelaxed oxide slab energies, (iv) the relaxed oxide slab energies, and (v) the surface area.

Interface structures	Cohesive energy of oxide slab (eV/molecule)	Number of molecules in oxide slab	Energy of unrelaxed oxide slab (eV)	Energy of relaxed oxide slab (eV)	Lattice constant a (Å)	Lattice constant b (Å)	Surface energy of oxide slab ($\text{eV}\cdot\text{Å}^{-2}$)
$\text{Al}(100)/\text{CrO}_3(100)$	-31.408	16	-500.620	-500.734	8.42	11.48	0.009
$\text{Al}(100)/\text{Cr}_2\text{O}_3(100)$	-43.110	18	-719.891	-743.478	7.86	14.67	0.039
$\text{Al}(110)/\text{CrO}_3(100)$	-31.408	16	-500.620	-500.735	8.42	11.48	0.009
$\text{Al}(110)/\text{Cr}_2\text{O}_3(100)$	-43.110	18	-719.892	-743.479	7.86	14.67	0.039
$\text{Al}(111)/\text{CrO}_3(100)$	-31.408	24	-750.932	-751.102	25.25	5.74	0.009
$\text{Al}(111)/\text{Cr}_2\text{O}_3(100)$	-43.110	18	-719.892	-743.478	14.67	7.86	0.039

face structures, the interface energy shows a substantial difference between the three Al substrate surface orientations, (100), (110), and (111). Namely, interface energy differences of $0.12 \text{ eV}\cdot\text{Å}^{-2}$ (130.4%) between the $\text{Al}(100)/\text{CrO}_3(100)$ and $\text{Al}(110)/\text{CrO}_3(100)$ interface structures, and $0.037 \text{ eV}\cdot\text{Å}^{-2}$ (40.2%) between $\text{Al}(100)/\text{CrO}_3(100)$ and $\text{Al}(111)/\text{CrO}_3(100)$ can be observed.

Conversely, the $\text{Al}/\text{Cr}_2\text{O}_3$ interface exhibits smaller energy variations across the different Al surface orientations. More specifically, a relatively small interface energy difference of $0.022 \text{ eV}\cdot\text{Å}^{-2}$ (17.2%) is found between the $\text{Al}(100)/\text{Cr}_2\text{O}_3(100)$ and $\text{Al}(110)/\text{Cr}_2\text{O}_3(100)$ interface structures, and an even smaller difference of $0.01 \text{ eV}\cdot\text{Å}^{-2}$ (7.8%) exists between $\text{Al}(100)/\text{Cr}_2\text{O}_3(100)$ and $\text{Al}(111)/\text{Cr}_2\text{O}_3(100)$. When comparing γ_j for Al/CrO_3 and $\text{Al}/\text{Cr}_2\text{O}_3$ for the same Al crystal orientation, the $\text{Al}/\text{Cr}_2\text{O}_3$ interface exhibits lower values than Al/CrO_3 for the $\text{Al}(100)$ and (111) planes. However, for the $\text{Al}(110)$ plane, $\text{Al}/\text{Cr}_2\text{O}_3$ displays a higher interface energy compared to Al/CrO_3 . Both Al/CrO_3 and $\text{Al}/\text{Cr}_2\text{O}_3$ yield the lowest interface energies when the Al surface orientation is along (110). Remarkably, the interface energies of these six interface structures display an inverse relationship with the adhesion work W_{ad} .

B. Analysis of interface atomic structures

To better understand the causes behind the quantitative variations observed in the adhesion work and the interface energies, W_{ad} and γ_i , here we provide a detailed analysis of the configurations of the six relaxed interface atomic structures considered (their unrelaxed counterparts are shown in Fig. 2). Fig. 3(a)-(f) includes snapshots of the final interface atomic structures of all six Al/CrO_3 and $\text{Al}/\text{Cr}_2\text{O}_3$ interface models.

Several dissimilarities can be observed in all Al/CrO_3 interface models, which makes them distinct from the $\text{Al}/\text{Cr}_2\text{O}_3$ ones. In $\text{Al}(100)/\text{CrO}_3(100)$, Fig. 3(a), oxygen atoms form bridges between Cr and Al atoms exactly at the interface through Al-O-Cr bonds. However, in $\text{Al}(110)/\text{CrO}_3(100)$, Fig.

TABLE VI. Calculated adhesion energies and interface energies of six Al/CrO_3 or $\text{Al}/\text{Cr}_2\text{O}_3$ structures. The interface energies are derived from the adhesion work, Al slab surface energy, and CrO_3 or Cr_2O_3 slab surface energies for each configuration. All values in $\text{eV}\cdot\text{Å}^{-2}$.

Interface structure	W_{ad}	γ_j
$\text{Al}(100)/\text{CrO}_3(100)$	0.184	-0.092
$\text{Al}(100)/\text{Cr}_2\text{O}_3(100)$	0.252	-0.128
$\text{Al}(110)/\text{CrO}_3(100)$	0.305	-0.212
$\text{Al}(110)/\text{Cr}_2\text{O}_3(100)$	0.273	-0.150
$\text{Al}(111)/\text{CrO}_3(100)$	0.217	-0.129
$\text{Al}(111)/\text{Cr}_2\text{O}_3(100)$	0.255	-0.138

3(c), four oxygen atoms prefer to dissociate from the Cr oxide and penetrate the Al slab to bond with metal atoms. This results in the formation of two molecules of Al_2O_3 (circled in Fig. 3(c)). Finally, in the $\text{Al}(111)/\text{CrO}_3(100)$ interface structure, shown in Fig. 3(e), two oxygen atoms break their bonds with chromium atoms and bond with aluminum atoms at the interface, forming Al_2O_3 molecules in the interfacial region (also circled). In the $\text{Al}/\text{Cr}_2\text{O}_3$ interface models shown in Figs. 3(b), 3(d), and 3(f), standard interfacial bonding is observed (Al-O-Cr) without any oxygen dissociation or formation of Al oxide.

Our results can then be construed in two different ways. First, it may appear that in metal(100)/oxide(100) configurations (regardless of the Cr oxide type), the metal and the oxide remain segregated. This could be due to the formation of a coherent interface characterized by a (100) || (100) orientation relation. However, it can also be argued that the atomic density mismatch between the Al substrate and the CrO_3 layer leads to epitaxial stresses [64] that may destabilize the interface, favoring the formation of aluminum oxide substructures.

To shed light on the operating mechanism behind the pen-

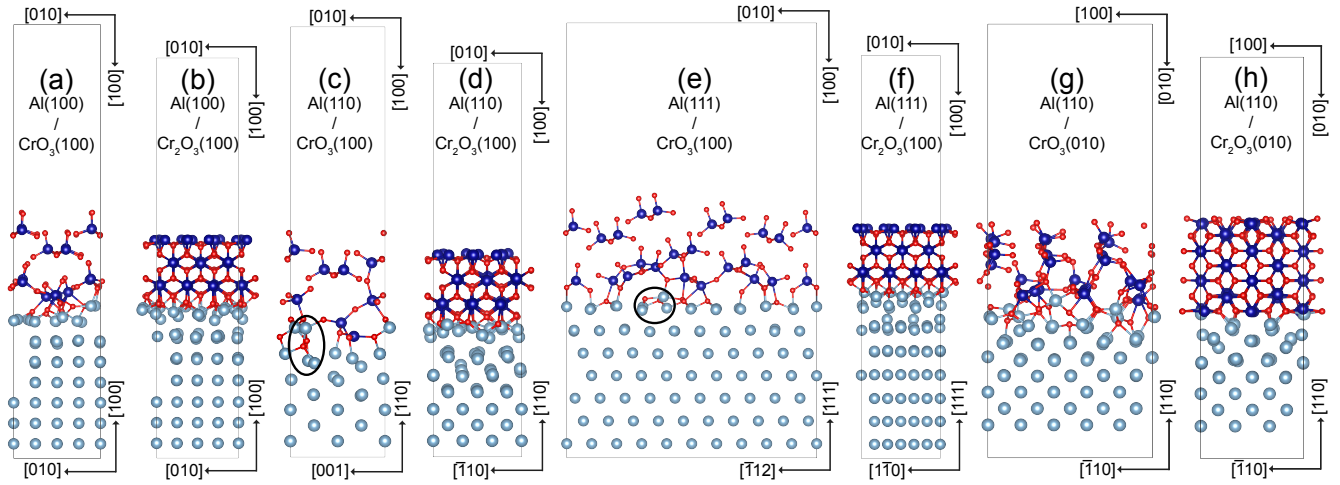


FIG. 3. Final atomic structures of the six Al/CrO₃(100) and Al/Cr₂O₃(100) interface models, along with two additional Al/Cr oxide (010) interface models. Gray-blue, red, and dark blue colored atoms represent aluminum, oxygen, and chromium atoms, respectively. The orientations of the Al, CrO₃, and Cr₂O₃ slabs are indicated within each interface model. In (c) and (e), the black circled portion highlights oxygen atoms breaking bonds with chromium atoms and bonding with aluminum atoms to form aluminum oxide bonds.

etration of oxygen atoms into the aluminum substrate and the formation of Al₂O₃ elements, a *shifted* Al(110)/CrO₃(100) model was created to change the contact site between the Cr oxide and the Al slab by displacing the oxide layer along the *b* (in-plane) direction by 1.1 Å. The initial and final interface atomic structures of the original and shifted Al(110)/CrO₃(100) interface models are illustrated in Fig. 4. Comparing the shifted and non-shifted Al(110)/CrO₃(100) interface models reveals a notable difference in the extent of oxygen penetration through the interface. The shifted model does not exhibit the penetration of oxygen atoms into the metallic layer to the extent that the non-shifted one does. As well, the two rows of Cr atoms immediately atop the Al atom row become highly distorted spatially, possibly due to Coulombic repulsion. This suggests that oxygen penetration may occur to compensate for the gap in charge density left by these atomic displacements. As such, the relative shift between the initial oxide and substrate slab positions may lead to atomic alignments that do not necessitate large Cr and O atom displacements in the direction normal to the surface.

These results invite the question of whether the formation of the interpenetrating Al-Cr oxide substructures or the formation of the Al-O-Al bond at the interface region improves adhesion and results in more stable interfaces. To that end, we list all four Al/CrO₃ interface models in Table VII and their values of W_{ad} , γ_{ij} , and the number of oxygen atoms that end up embedded in the Al slab (expressed as an areal concentration of atoms per nm²). The values between shifted and non-shifted Al(110)/CrO₃(100) interface models in the table unequivocally indicate that the oxygen traversing the interface from the Cr oxide to the Al substrate is behind the larger adhesion work (16.3%) and lower interface energies (32.6%) of the formed structures.

Aside from the non-shifted Al(110)/CrO₃(100) interface configuration, which exhibits oxygen penetration into the alu-

minium layer, all other Al/CrO₃ cases show only oxygen dissociation from Cr oxide to form the Al-O-Al bond at the interface region. From the data presented in Table VII, a linear relationship is observed between the areal density of oxygen atoms participating in the Al-O-Al bond formation at the interface region and the increase of W_{ad} and γ_{ij} . The fitted coefficients suggest that for every extra oxygen atom dissociated from the Cr oxide to form the Al-O-Al bond at the interface region, an increase of 11.9% in W_{ad} and a reduction of 23.2% in γ_{ij} are observed. This finding indicates that the variations in adhesion work W_{ad} and interface energy γ_{ij} of Al/CrO₃ interface models may be attributable to both the interpenetrating Al-Cr oxide substructures and the formation of the Al-O-Al bond at the interface region.

IV. DISCUSSION

A. Trivalent vs. hexavalent Cr oxide considerations

One of the key questions that we aim to answer with the calculations presented in this paper is whether trivalent chromium oxide can adhere to aluminum metal substrates more strongly than their hexavalent Cr oxide counterparts. Inspection of the results in Table VI reveals average adhesion works of 0.260 eV·Å⁻² for Cr₂O₃ (trivalent) versus 0.235 eV·Å⁻² for CrO₃ (hexavalent). This amounts to a difference of approximately 10% in favor of the trivalent Cr oxide. While the difference is small, our calculations suggest that there might exist a slight advantage in bonding strength when replacing Cr⁶⁺ with Cr³⁺ in the protective oxide layers coating aluminum surfaces. This is corresponded by a similar trend in the interface energies. It is important to note that our simulations represent ideal surfaces at 0 K, with no consideration of realistic features such as the presence of oxygen in-

TABLE VII. Adhesion work, interface energy, and areal density of transferred oxygen atoms for four Al/CrO₃ interface models. The increments in adhesion work and interface energy (in percentages) are listed for each structure, using the Al(100)/CrO₃(100) interface case as the reference.

Interface structure	W_{ad} (eV·Å ⁻²)	γ_{ij} (eV·Å ⁻²)	O-atom areal concentration (nm ⁻²)
Al(100)/CrO ₃ (100)	0.184 (+0.00%)	-0.092 (+0.00%)	0.00
Al(111)/CrO ₃ (100)	0.217 (+17.9%)	-0.129 (+40.2%)	1.38
Shifted Al(110)/CrO ₃ (100)	0.275 (+49.5%)	-0.182 (+97.8%)	4.14
Al(110)/CrO ₃ (100)	0.305 (+65.8%)	-0.212 (+130.4%)	4.14

terstitials, vacancies, grain boundaries, or surface roughness.

CrO₃ layers bonded to Al(110) and Al(111) slabs experience a transfer of oxygen atoms to the metal substrate. This results in more stable interfaces and higher adhesion works compared with Al(100) surface and is likely related to the more open structure of (110) and (111) surfaces, which facilitates O-atom penetration. As well, we do not discount the possibility that this may be driven by epitaxial stresses caused by the large atomic density difference between CrO₃ and Al. These stresses are generally represented by the Pilling-Bedforth parameter, which will be discussed below. However, this variability leads to larger differences in energy and work for the different interface orientations. Additionally, the open crystal structure of CrO₃ is likely to enhance oxygen transport through it, increasing its oxidizing power.

A distinctive feature separating Al/Cr₂O₃ from Al/CrO₃ structures is the homogeneous bonding configuration observed in Al/Cr₂O₃. This results in unmixed metal/oxide layers, with all the oxygen retained on the oxide side simply acting as the bridge between Al and Cr atoms. This results in relatively small differences across the different interface orientations, both in the calculated adhesion works, W_{ad} , and interface energies, γ_{ij} . The coherent interface bonding and rigidity of the Cr₂O₃ crystal structure significantly reduces mass transport within it, making Cr₂O₃ chemically inert under most conditions. Consequently, we conjecture that Cr₂O₃ will display superior performance as a protective layer on aluminum surfaces.

While the calculations presented in this paper pertain only to static oxide/metal interface properties, recent experimental evidence in Ni-Cr alloys indicates that there exists a connection between the stability of the interface (quantified by a low interface energy and/or a high adhesion work) and the associated initial oxidation rate (i.e., prior to the onset of steady-state oxidation, which is controlled primarily by oxygen diffusion), which tends to be slower the more stable the interface is [65]. Following this logic, our results in Table VI for the Al/CrO₃ interface suggest that the Al(110) substrate orientation would lead to slower initial oxidation rates than the Al(100) and Al(111) orientations.

B. Effect of chemical arrangement of oxygen atoms

Given that we employed both O-terminal CrO₃ and Cr-terminal Cr₂O₃ slabs for model construction and simulations, it is essential to evaluate the influence of the terminating atom on interface stability. To this end, we generated and analyzed a new Al(100)/Cr₂O₃(100) model with an O-terminal surface. Using the parameters specific to this configuration, we calculated the adhesion work following eq. (2), with results and parameters summarized in Table VIII. When compared to the Cr-terminal Al(100)/Cr₂O₃(100) model (adhesion work listed in Table II), the O-terminal model exhibits a slightly higher adhesion work, suggesting a minor improvement in interface stability. However, given the minimal difference, the effect of the terminating atom on overall interface stability can be considered negligible.

The influence of different terminal atoms raises another interesting question: do varying crystallographic orientations of Cr oxides affect interface stability? To investigate this, we generated and calculated two new models of CrO₃ and Cr₂O₃ with the (010) orientation, paired with Al(110) substrates. The adhesion work for these two models was computed using eq. (2) and the results listed in Table VIII. When compared with the Cr oxide models with (100) orientations in Table II, the CrO₃(010) model exhibits a slightly lower adhesion work, whereas the Cr₂O₃(010) model shows a significantly reduced value (≈ 0.1 eV·Å⁻² lower). The final interface atomic structures of the two new models are shown in Figs. 3(g) and 3(h). In Fig. 3(g), the CrO₃(010) model exhibits oxygen dissociation from the Cr oxide layer, followed by oxygen transport into the metallic layer to form Al₂O₃ at the interface. In contrast, Fig. 3(h) shows the Cr₂O₃(010) model with a coherent interface structure. Both CrO₃(010) and Cr₂O₃(010) models demonstrate interface atomic structures similar to their respective (100) Cr oxide models when paired with the Al(110) substrate. To further understand the mechanism behind how different Cr oxide orientations influence interface stability, we resort to calculating the Pilling-Bedworth (P-B) ratio (R_{P-B}), a parameter commonly used to quantify oxide-metal misfit stresses [66, 67]:

$$R_{P-B} = \frac{M_{\text{ox}} \cdot \rho_{\text{m}}}{n \cdot M_{\text{m}} \cdot \rho_{\text{ox}}} \quad (6)$$

where M_{ox} and M_{m} are the molar masses of Cr oxide and

TABLE VIII. Calculated adhesion work of three Al/CrO₃ or Al/Cr₂O₃ interface models using the relaxed interface model energy, single strained Al slab energy, single CrO₃ or Cr₂O₃ slab energy, and interface dimensions along the *a* and *b* directions.

Interface structure	Combined energy (eV)	Energy of Al slab (eV)	Energy of oxide slab (eV)	Lattice constant <i>a</i> (Å)	Lattice constant <i>b</i> (Å)	Adhesion work (eV·Å ⁻²)
O-terminal Al(100)/Cr ₂ O ₃ (100)	-1356.9	-433.2	-890.7	7.86	14.67	0.287
Al(110)/CrO ₃ (010)	-1194.0	-398.5	-750.5	11.48	14.27	0.275
Al(110)/Cr ₂ O ₃ (010)	-1527.8	-315.8	-1189.6	9.08	14.67	0.168

Al, respectively, ρ_{ox} and ρ_{m} are the densities of Cr oxide and Al, respectively, and n is the number of surface Al atoms required to balance the formation of each Cr oxide molecule. In calculating the P-B ratio, we used the bulk densities of Cr oxide and Al obtained from separate supercell calculations. This approach is consistent with the conventional definition of the P-B ratio in oxidation studies, which uses bulk properties to broadly characterize oxide-metal misfit stresses and avoids complexities from local interfacial distortions. Following eq. (6), the P-B ratio of the six Cr oxide models with (100) surface orientation and the two Cr oxide models with (010) surface orientation were calculated for different Al orientations, as listed in Table IX. Notably, the P-B ratio for the CrO₃(010) model is slightly lower than that of the CrO₃(100) model. In contrast, the P-B ratio for the Cr₂O₃(010) model is significantly lower than that for the Cr₂O₃(100) model. These P-B ratio trends align with the adhesion work trends listed in Table IX, suggesting that the P-B ratio is a satisfactory metric to predict the stability of different Cr oxide orientations. To further investigate the influence of the P-B ratio on Al/Cr oxide stability, we plot all the P-B ratio values versus adhesion work data listed in Table IX in Fig. 5. With the same Al(110) substrate (orange-colored), the P-B ratio correlates with interface stability regardless of Cr oxide type and orientation. However, for Al(100) (blue-colored) and Al(111) (green-colored) substrates, the P-B ratio correlates inversely with interface stability. For the same CrO₃(100) models (solid dots), the relationship between the P-B ratio and adhesion work for different Al orientation substrates is unclear. In contrast, for the same Cr₂O₃(100) models (solid triangle), the adhesion work for different Al orientation substrates is similar, which is independent of the P-B ratio. Therefore, we conclude that the crystallographic orientations of the Cr oxide significantly influence interface stability, in addition to the dependence due to the metal substrate orientation.

V. SUMMARY AND CONCLUSIONS

We finalize with our most important conclusions:

- We have used DFT calculations to calculate the adhesion work and interface energies between trivalent (Cr₂O₃) and hexavalent (CrO₃) chromium oxide and aluminum metal substrates with different crystallographic orientations.

TABLE IX. Calculated Pilling-Bedworth (P-B) ratios and corresponding adhesion work for six Cr oxide models with (100) plane and two Cr oxide models with (010) plane, interfacing with Al substrates of varying crystallographic orientations. P-B ratios are computed based on eq. (6).

Interface structure	R_{P-B}	W_{ad} (eV·Å ⁻²)
Al(100)/CrO ₃ (100)	1.235	0.184
Al(100)/Cr ₂ O ₃ (100)	1.092	0.252
Al(110)/CrO ₃ (100)	1.852	0.305
Al(110)/Cr ₂ O ₃ (100)	1.456	0.273
Al(111)/CrO ₃ (100)	1.111	0.217
Al(111)/Cr ₂ O ₃ (100)	0.971	0.255
Al(110)/CrO ₃ (010)	1.482	0.275
Al(110)/Cr ₂ O ₃ (010)	0.971	0.168

- We find that Al/Cr₂O₃ interface energies display a relatively weak dependence on metal substrate orientation. All the configurations considered here were characterized by clearly demarcated oxide and metallic layers with no dissociation of oxygen atoms to the metal substrate.
- The relaxed Al/CrO₃ interfaces show instead propensity for oxygen transport to the metallic layer, with the local formation of Al₂O₃ molecules observed. This results in wider differences in the interface energies and adhesion work across the different crystal orientations considered.
- On average, trivalent Cr oxide interfaces possess lower interface energies and higher adhesion works than those formed by hexavalent Cr oxide with the metal.
- These findings provide valuable insights into the potential of Cr₂O₃ coatings as a viable alternative to CrO₃ in environmental applications, offering improved corrosion protection while mitigating environmental concerns associated with CrO₃. Our study contributes to the ongoing efforts to develop sustainable corrosion protection solutions in the aerospace and marine industries and paves the way for further exploration of envi-

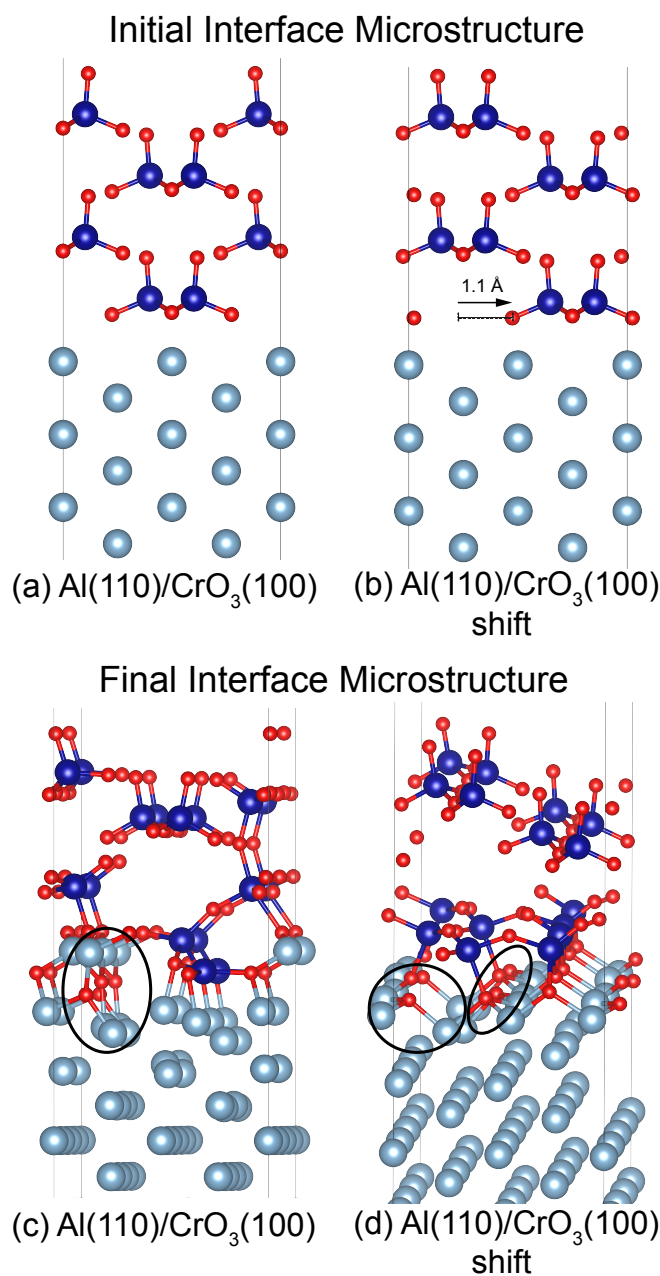


FIG. 4. The initial and final interface atomic structures of Al(110)/CrO₃(100) and shifted Al(110)/CrO₃(100) models. (a) Al(110)/CrO₃(100) model initial interface atomic structure. (b) Shifted Al(110)/CrO₃(100) model initial interface atomic structure. In (b), the shift vector is indicated. (c) Al(110)/CrO₃(100) model final interface atomic structure. (d) Shifted Al(110)/CrO₃(100) model final interface atomic structure. In (c) and (d), the black circled portion highlights oxygen atoms breaking bonds with chromium and forming aluminum oxide.

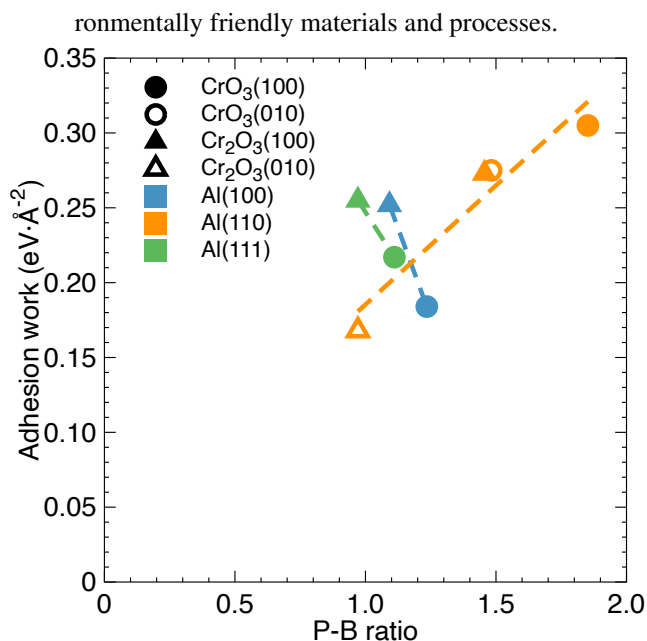


FIG. 5. Relationship between the Pilling-Bedworth (P-B) ratio and adhesion work various Al/Cr oxide interface models. Data points are shaped according to the type of Cr oxide and colored based on the Al substrate orientation. The combination of shape and color represents each specific Al/Cr oxide interface model. Dashed lines are intended as visual guides to the data.

ACKNOWLEDGMENTS

We gratefully acknowledge support from PPG Inc. under their project on modeling of trivalent chrome pretreatments. Special thanks to Eric Morris and Krishnan Chari for encouraging this research, and for helpful discussions. This work utilized computational resources from the Argonne Leadership Computing Facility, a user facility of the U.S. Department of Energy (DOE) Office of Science at Argonne National Laboratory, with support from the U.S. DOE Office of Science's Advanced Scientific Computing Research Program under Contract No. DE-AC02-06CH11357.

[1] T. Dursun and C. Soutis, Recent developments in advanced aircraft aluminium alloys, *Materials & Design* (1980-2015) **56**,

862 (2014).

[2] S. Li, X. Yue, Q. Li, H. Peng, B. Dong, T. Liu, H. Yang, J. Fan,

- S. Shu, F. Qiu, and Q. Jiang, Development and applications of aluminum alloys for aerospace industry, *Journal of Materials Research and Technology* **27**, 944 (2023).
- [3] P. A. B. Machado, J. M. do Vale Quaresma, A. Garcia, and C. A. dos Santos, Investigation on machinability in turning of as-cast and t6 heat-treated al-(3, 7, 12%)si-0.6%mg alloys, *Journal of Manufacturing Processes* **75**, 514 (2022).
- [4] J. C. Williams and E. A. Starke, Progress in structural materials for aerospace systems, *Acta Materialia* **51**, 5775 (2003).
- [5] O. F. Hosseinabadi and M. R. Khedmati, A review on ultimate strength of aluminium structural elements and systems for marine applications, *Ocean Engineering* **232**, 109153 (2021).
- [6] M. A. Wahid, A. N. Siddiquee, and Z. A. Khan, Aluminum alloys in marine construction: characteristics, application, and problems from a fabrication viewpoint, *Marine Systems & Ocean Technology* **15**, 70 (2020).
- [7] C. Ungureanu, S. Das, and I. Jawahir, Life-cycle cost analysis: aluminum versus steel in passenger cars, TMS (the minerals, metals & materials society) **1**, 11 (2007).
- [8] R. Roth, J. Clark, and A. Kelkar, Automobile bodies: Can aluminum be an economical alternative to steel?, *Jom* **53**, 28 (2001).
- [9] Z. Ahmad, *Principles of Corrosion Engineering and Corrosion Control* (Butterworth-Heinemann, 2006).
- [10] M. Schütze, D. Wieser, and R. Bender, *Corrosion Resistance of Aluminium and Aluminium Alloys* (Wiley, 2010).
- [11] K. Dychtoń, M. Wierzbńska, B. Kościelniak, A. Oblój, M. Wojnicki, and P. Kwolek, The role of the oxide layer in the corrosion of aluminium in acidic solutions, *Materials and Corrosion* **75**, 471–488 (2024).
- [12] S. E. Potts, L. Schmalz, M. Fenker, B. Díaz, J. Świątowska, V. Maurice, A. Seyeux, P. Marcus, G. Radnóczy, L. Tóth, and W. M. M. Kessels, Ultra-thin aluminium oxide films deposited by plasma-enhanced atomic layer deposition for corrosion protection, *Journal of The Electrochemical Society* **158**, C132 (2011).
- [13] Y. Liu, Z. Wang, and W. Ke, Study on influence of native oxide and corrosion products on atmospheric corrosion of pure al, *Corrosion Science* **80**, 169 (2014).
- [14] R. Deuis, C. Subramanian, and J. Yellup, Abrasive wear of aluminium composites—a review, *Wear* **201**, 132 (1996).
- [15] S. Mezlini, P. Kapsa, C. Henon, and J. Guilleminet, Abrasion of aluminium alloy: effect of subsurface hardness and scratch interaction simulation, *Wear* **257**, 892 (2004).
- [16] H. H. Uhlig and R. W. Revie, *Corrosion and corrosion control. Third edition* (Wiley, 1985).
- [17] X. Zhang, C. van den Bos, W. Sloof, A. Hovestad, H. Terry, and J. de Wit, Comparison of the morphology and corrosion performance of cr(vi)- and cr(iii)-based conversion coatings on zinc, *Surface and Coatings Technology* **199**, 92 (2005).
- [18] J. Zhao, L. Xia, A. Sehgal, D. Lu, R. McCreery, and G. Frankel, Effects of chromate and chromate conversion coatings on corrosion of aluminum alloy 2024-t3, *Surface and Coatings Technology* **140**, 51 (2001).
- [19] F. Peltier and D. Thierry, Review of cr-free coatings for the corrosion protection of aluminum aerospace alloys, *Coatings* **12**, 518 (2022).
- [20] J. Kloet, W. Schmidt, A. Hassel, and M. Stratmann, The role of chromate in filiform corrosion inhibition, *Electrochimica Acta* **48**, 1211 (2003).
- [21] J. Yang, M. Steinbrück, C. Tang, M. Große, J. Liu, J. Zhang, D. Yun, and S. Wang, Review on chromium coated zirconium alloy accident tolerant fuel cladding, *Journal of Alloys and Compounds* **895**, 162450 (2022).
- [22] R. Twite and G. Bierwagen, Review of alternatives to chromate for corrosion protection of aluminum aerospace alloys, *Progress in Organic Coatings* **33**, 91 (1998).
- [23] A. Wang, K. De Silva, M. Jones, P. Robinson, G. Larribe, and W. Gao, Anticorrosive coating systems for marine propellers, *Progress in Organic Coatings* **183**, 107768 (2023).
- [24] S. Hesamedini, Trivalent chromium conversion coatings, *Journal of Coatings Technology and Research* **16**, 623–641 (2019).
- [25] Y. Guo and G. Frankel, Characterization of trivalent chromium process coating on aa2024-t3, *Surface and Coatings Technology* **206**, 3895 (2012).
- [26] J.-T. Qi, T. Hashimoto, J. Walton, X. Zhou, P. Skeldon, and G. Thompson, Trivalent chromium conversion coating formation on aluminium, *Surface and Coatings Technology* **280**, 317 (2015).
- [27] M. Cruz and S. E. Rodil, Improving the corrosion resistance of aluminum alloy (aa7075) using amorphous chromium oxide coatings, *Materials Letters* **278**, 128459 (2020).
- [28] S. Huang, R. Kerr, S. Murphy, M. R. Gilbert, and J. Marian, Multilayer interface tracking model of pure tungsten oxidation, *Modelling and Simulation in Materials Science and Engineering* **30**, 085015 (2022).
- [29] D. Jennison, C. Verdozzi, P. Schultz, and M. Sears, Ab initio structural predictions for ultrathin aluminum oxide films on metallic substrates, *Physical Review B* **59**, R15605 (1999).
- [30] M.-H. Chen, B. Puchala, and A. Van der Ven, High-temperature stability of δ -zro, *Calphad* **51**, 292 (2015).
- [31] A. Eichler, Modeling oxide-metal interfaces from density-functional theory: Platinum adsorption on tetragonal zirconia, *Physical Review B* **68**, 205408 (2003).
- [32] B. Cantor, *The Equations of Materials* (Oxford University Press, 2020).
- [33] W. Liu, J. C. Li, W. T. Zheng, and Q. Jiang, NiAl(110)/Cr(110) interface: A density functional theory study, *Phys. Rev. B* **73**, 205421 (2006).
- [34] S. Suresh, *Fatigue of Materials*, 2nd ed. (Cambridge University Press, 1998).
- [35] M. W. Finnis, The theory of metal - ceramic interfaces, *Journal of Physics: Condensed Matter* **8**, 5811 (1996).
- [36] Y.-D. Zhou and Z.-Y. Zhao, Interfacial structure and properties of tio2 phase junction studied by dft calculations, *Applied Surface Science* **485**, 8 (2019).
- [37] M. Fathalian, E. Postek, and T. Sadowski, Mechanical and electronic properties of al(111)/6h-sic interfaces: A dft study, *Molecules* **28** (2023).
- [38] W. Xu, A. P. Horsfield, D. Wearing, and P. D. Lee, First-principles calculation of mg/mgo interfacial free energies, *Journal of Alloys and Compounds* **650**, 228 (2015).
- [39] J. Reedijk and K. Poeppelmeier, *Comprehensive Inorganic Chemistry III, Third Edition* (Elsevier, 2023).
- [40] J. van der Merwe, Interfacial energy: bicrystals of semi-infinite crystals, *Progress in Surface Science* **67**, 365 (2001).
- [41] Y. Wang, X. Liu, Q. Yang, Y. Liu, Z. Li, B. Guo, H. Mao, R. D. K. Misra, and H. Xu, First principles calculation of interfacial stability, energy, and elemental diffusional stability of Fe (111)/Al2O3 (0001) interface, *AIP Advances* **9**, 125313 (2019).
- [42] M. Christensen, S. Dudiy, and G. Wahnström, First-principles simulations of metal-ceramic interface adhesion: Co/wc versus co/tic, *Phys. Rev. B* **65**, 045408 (2002).
- [43] Q. Li, M. Rellán-Piñeiro, N. Almora-Barrios, M. Garcia-Ratés, I. N. Remediakis, and N. López, Shape control in concave metal nanoparticles by etching, *Nanoscale* **9**, 13089 (2017).
- [44] G. Kresse and J. Hafner, Ab initio molecular dynamics for liquid metals, *Phys. Rev. B* **47**, 558 (1993).

- [45] G. Kresse and J. Hafner, Ab initio molecular-dynamics simulation of the liquid-metal–amorphous-semiconductor transition in germanium, *Phys. Rev. B* **49**, 14251 (1994).
- [46] G. Kresse and J. Hafner, Norm-conserving and ultrasoft pseudopotentials for first-row and transition elements, *Journal of Physics: Condensed Matter* **6**, 8245 (1994).
- [47] G. Kresse and J. Furthmüller, Efficiency of ab-initio total energy calculations for metals and semiconductors using a plane-wave basis set, *Computational Materials Science* **6**, 15 (1996).
- [48] G. Kresse and J. Furthmüller, Efficient iterative schemes for ab initio total-energy calculations using a plane-wave basis set, *Phys. Rev. B* **54**, 11169 (1996).
- [49] G. Kresse and D. Joubert, From ultrasoft pseudopotentials to the projector augmented-wave method, *Phys. Rev. B* **59**, 1758 (1999).
- [50] M. Hacene, A. Anciaux-Sedrakian, X. Rozanska, D. Klahr, T. Guignon, and P. Fleurat-Lessard, Accelerating vasp electronic structure calculations using graphic processing units, *Journal of Computational Chemistry* **33**, 2581 (2012).
- [51] M. Hutchinson and M. Widom, Vasp on a gpu: Application to exact-exchange calculations of the stability of elemental boron, *Computer Physics Communications* **183**, 1422 (2012).
- [52] K. Momma and F. Izumi, *VESTA3* for three-dimensional visualization of crystal, volumetric and morphology data, *Journal of Applied Crystallography* **44**, 1272 (2011).
- [53] J. P. Perdew, K. Burke, and M. Ernzerhof, Generalized gradient approximation made simple, *Phys. Rev. Lett.* **77**, 3865 (1996).
- [54] P. Geng, S. Zybin, S. Naserifar, and I. Goddard, William A., Quantum mechanics based non-bonded force field functions for use in molecular dynamics simulations of materials and systems: The nitrogen and oxygen columns, *The Journal of Chemical Physics* **159**, 164104 (2023).
- [55] S. Grimme, S. Ehrlich, and L. Goerigk, Effect of the damping function in dispersion corrected density functional theory, *Journal of Computational Chemistry* **32**, 1456 (2011).
- [56] D. Zagorac, H. Müller, S. Ruehl, J. Zagorac, and S. Rehme, Recent developments in the Inorganic Crystal Structure Database: theoretical crystal structure data and related features, *Journal of Applied Crystallography* **52**, 918 (2019).
- [57] L. Vitos, A. Ruban, H. Skriver, and J. Kollár, The surface energy of metals, *Surface Science* **411**, 186 (1998).
- [58] A. Patra, J. E. Bates, J. Sun, and J. P. Perdew, Properties of real metallic surfaces: Effects of density functional semilocality and van der waals nonlocality, *Proceedings of the National Academy of Sciences* **114**, E9188 (2017).
- [59] M. N. Magomedov, Temperature and pressure dependences of the surface energy for a macro- and nanocrystal, *Physics of the Solid State* **63**, 1465–1479 (2021).
- [60] K. C. Mills and Y. C. Su, Review of surface tension data for metallic elements and alloys: Part 1 – pure metals, *International Materials Reviews* **51**, 329 (2006).
- [61] V. K. Kumikov and K. B. Khokonov, On the measurement of surface free energy and surface tension of solid metals, *Journal of Applied Physics* **54**, 1346 (1983).
- [62] W. Tyson and W. Miller, Surface free energies of solid metals: Estimation from liquid surface tension measurements, *Surface Science* **62**, 267 (1977).
- [63] H. L. Skriver and N. M. Rosengaard, Surface energy and work function of elemental metals, *Phys. Rev. B* **46**, 7157 (1992).
- [64] Known as ‘Pilling-Bedworth stresses’ in the context of M/MOx interfaces (where ‘M’ refers to the metal) [66, 67].
- [65] S. Li, L. Yang, J. Christudasjustus, N. R. Overman, B. D. Wirth, M. L. Sushko, P. Simonnin, D. K. Schreiber, F. Gao, and C. Wang, Selective atomic sieving across metal/oxide interface for super-oxidation resistance, *Nature Communications* **15**, 6149 (2024).
- [66] C. Xu and W. Gao, Pilling-bedworth ratio for oxidation of alloys, *Material Research Innovations* **3**, 231 (2000).
- [67] M. Reyes, A. Aryanfar, S. W. Baek, and J. Marian, Multilayer interface tracking model of zirconium clad oxidation, *Journal of Nuclear Materials* **509**, 550 (2018).